nature communications

Article

https://doi.org/10.1038/s41467-024-52632-8

Metasurface-enabled broadband multidimensional photodetectors

Received: 6 June 2024

Accepted: 17 September 2024

Published online: 27 September 2024

Check for updates

Hao Jiang[1,8], Yinzhu Chen[2,3,8], Wenyu Guo[1,4,5,6], Yan Zhang[1], Rigui Zhou[4,5], Mile Gu[1,6], Fan Zhong[3], Zhenhua Ni[3], Junpeng Lu[3] ✉, Cheng-Wei Qiu[2] ✉ & Weibo Gao[1,6,7] ✉

Light encodes multidimensional information, such as intensity, polarization, and spectrum. Traditional extraction of this light information requires discrete optical components by subdividing the detection area into many "one-to-one" functional pixels. The broadband photodetection of high-dimensional optical information with a single integrated on-chip detector is highly sought after, yet it poses significant challenges. In this study, we employ a metasurface-assisted graphene photodetector, enabling to simultaneously detect and differentiate various polarization states and wavelengths of broadband light (1-8 μm) at the wavelength prediction accuracy of 0.5 μm. The bipolar polarizability empowered by this design allows to decouple multidimensional information (encompassing polarization and wavelength), which can be achieved by encoding vectorial photocurrents with varying polarities and amplitudes. Furthermore, cooperative multiport metasurfaces are adopted and boosted by machine learning techniques. It enables precise spin-wavelength differentiation over an extremely broad wavelength range (1-8 μm). Our innovation offers a recipe for highly compact and high-dimensional spectral-polarization co-detection.

Extracting multidimensional information from light is crucial for achieving holistic understanding, multilayer perceptron and maneuverability of optical information, such as in optical sensing, optical communication and optical computing[1–5]. However, detecting information other than light intensity typically requires the collaborative action of massive optical components[6–8]. On-chip integrated optoelectronic detection technology has the capability to unleash its spatial degrees of freedom, thereby offering possibilities for the design of the next generation of miniaturized optoelectronic chips[9–20]. However, most current endeavors are limited to achieving, at most, two-dimensional parameter detection, such as spectral detection (wavelength and intensity)[21–24] or polarization spectrum detection (polarization and intensity)[2,25,26]. Detecting spectra with higher-dimensional parameters poses even greater challenges.

Recently, twisted bilayer graphene with individual biased gatings has been successfully employed and demonstrated simultaneous photodetection of light's polarization states at two wavelengths (5 μm and 7.7 μm)[27]. More recently, the dispersion-assisted high-dimensional photodetector is shown to detect full polarization sates and 6 wavelengths without resorting to metasurfaces or moire low-dimensional materials[28]. However, this method still suffers from spatial resolution

[1]School of Physical and Mathematical Sciences, Nanyang Technological University, Singapore 639798, Singapore. [2]Department of Electrical and Computer Engineering, National University of Singapore, Singapore 117583, Singapore. [3]Key Laboratory of Quantum Materials and Devices of Ministry of Education, School of Physics, Southeast University, Nanjing 211189, China. [4]College of Information Engineering, Shanghai Maritime University, Shanghai 201306, China. [5]Research Center of Intelligent, Information Processing and Quantum Intelligent Computing, Shanghai 201306, China. [6]Centre for Quantum Technologies, National University of Singapore, Singapore, Singapore. [7]School of Electrical and Electronic Engineering, Nanyang Technological University, Singapore, Singapore. [8]These authors contributed equally: Hao Jiang, Yinzhu Chen. ✉e-mail: phyljp@seu.edu.cn; chengwei.qiu@nus.edu.sg; wbgao@ntu.edu.sg

due to the use of commercial CMOS camera array, and the corresponding spectral bands are also limited by intrinsic dispersion of the thin film atop of the CMOS camera, and it may be elusive to extend this recipe into mid-infrared regimes due to the lack of proper dispersions as in the visible-light counterpart[28]. The involvement of commercial CMOS detectors inevitably requires N-detectors for mapping N-dimensional input states to the ouput, resulting in sacrifice in spatial resolution even with the assistance of machine learning algorithms[29].

Here, we employ a metasurface-assisted graphene photodetector, enabling to simultaneously detect and differentiate various polarization states and wavelengths of broadband light (1–8 μm) at the wavelength prediction accuracy of 0.5 μm. The bipolar polarizability empowered by this design allows to decouple multidimensional information (encompassing polarization and wavelength), which can be achieved by encoding vectorial photocurrents with varying polarities and amplitudes. Furthermore, cooperative multiport metasurfaces are adopted and boosted by machine learning techniques. It enables precise spin-wavelength differentiation over an extremely broad wavelength range (1–8 μm). This design only requires a single measurement of each port of device to detect broadband high-dimensional optical information, thereby balancing both temporal and spatial resolutions. This provides a solution for ultra-compact, high-dimensional spectral detection. Importantly, the design of our core sensor does not require additional degrees of freedom such as twists, heterojunctions, or gate control. Instead, it can be achieved by relatively simple and mature metasurface designs combined with graphene films, ensuring reliability in information detection, processing, and stability.

Results

Approach of intelligent high-dimensional spectral detection

As far, high-dimensional spectral detection is limited to achieving two-dimensional parameter detection (spectrum-intensity detection or polarization-intensity detection), as depicted by the sliced sections in the left subplot of Fig. 1a. In ubiquitous natural scenarios, a light field to be detected may exhibit arbitrarily varying polarizations and intensities across a wide range of wavelengths, as depicted by the curved surface in Fig. 1a. This essentially necessitates the establishment of a high-dimensional photodetector capable of fully characterizing the three-dimensional parametric coordinate space and accurately describing any light field. Therefore, there is an urgent demand for sensor designs that can effectively detect and differentiate high-dimensional information simultaneously.

In our design proposal, we propose to apply machine learning to process signals collected by sensors with high-dimensional detection capabilities, aiming to achieve high-dimensional spectral detection, as depicted in the right subplot of Fig. 1a. The core sensor is designed to utilize a set of integrated dual-arm plasmonic nanostructures on a graphene platform to detect light with different polarization states in two wavelength bands. Light with different wavelengths and polarization states can lead to photovoltage signals with distinct polarities and amplitudes. The bidirectional and polarizability detection induced by this design enables the decoupling of multidimensional information, encompassing polarization and wavelength. By employing a photovoltage with positive and negative polarities as new signal dimensions, we demonstrate significant resolution capabilities in both wavelength and polarization states. As an extension, the fabrication of dual-arm plasmonic nanostructures with different designs for three-port devices enables polarization detection in three wavelength bands, spanning from the near-infrared to mid-infrared (1.55 μm, 4 μm and 7 μm) regions, as depicted in Fig. 1b.

Furthermore, leveraging machine learning techniques to learn from and reconstruct the collected three-port photocurrent data. Multiport cooperative interactions and machine learning techniques enable precise differentiation of both the wavelength and polarization information of light over an extremely broad wavelength range. Finally, when light with unknown wavelength and polarization information is incident upon the device, the resulting photocurrent signals are input into the established photocurrent model for sampling. Through this process, the wavelength and polarization information of the incoming light signal can be determined, as demonstrated in Fig. 1c. We showcase the wavelength prediction accuracy can reach 0.5 μm over an ultra-wide wavelength range of 1–8 μm.

Nanoantennas for multidimensional information detection

Here, the core design principle of multidimensional spectral detection lies in the realization of a sensor with the capability to resolve both wavelength and polarization information. Typically, we take the example of circularly polarized light with complex polarization information, and endeavor to implement detection of both wavelength and spin information using graphene-based metasurface. A schematic of the designed metasurface-mediated photodetector is shown in Fig. 2a. The metasurface consists of dual-arm plasma structures as meta-atoms on top of graphene flakes. The device morphology characterization is shown in Supplementary Fig. 1 and Supplementary Fig. 2 of Supplementary Note 1. Two different wavelengths (λ_1 and λ_2) of light pass through a quarter-wave plate (QWP), transform into CPL with distinct chirality, and then illuminate the device. Therefore, four types of combined signals with different wavelengths and circular polarization information can be obtained: λ_1 LCP, λ_1 RCP, λ_2 LCP, and λ_2 RCP. The design principle of our proposed plasmonic nanostructures is illustrated on the right side of Fig. 2a. The length of the dual arms determines the resonance wavelengths at λ_1 and λ_2. Four types of light will interact with the four-sided resonances of a dual-arm nanostructure, giving rise to four distinct asymmetric resonance modes[30–33]. The simulated near-field distribution of the structure and its photocurrent density distribution are depicted in Fig. 2b. Due to the gapless properties of graphene, we consider the photocurrents to originate from the local heating of light and subsequent heat flow via non-uniformities in the Seebeck coefficient, S, with the direction and amplitude determined by the gradient of S, that is, $I_{ph} \propto |E^2| \cdot \vec{\nabla} S$, where E is the amplitude of light in the local area[34–38]. Therefore, light with different wavelengths and circular polarization states will generate vector photocurrents of varying magnitudes and directions. The local optical response from nanoantennas can effectively contribute to external circuits in a nonlocal manner, thereby achieving a cascaded total photocurrent with distinctions in polarity and magnitude. The near-field mode and photocurrent analysis of the dual-arm nanostructure are explained in Supplementary Figs. 3–11 of Supplementary Note 2.

For the size of our designed nanoantennas, during simulation, we discovered that varying the length of the central axis of the double-arm nanoantenna can make the device sensitive to linearly polarized light as well. We can write the general expression for a polarization-dependent photoresponse: $V_{\mathrm{ph}} = R_0 \cdot S_0 + R_1 \cdot S_1 + R_2 \cdot S_2 + R_3 \cdot S_3$, with the $R_{0,1,2,3}$ as the respective responsivities to the four Stoke parameters, $S_{0,1,2,3}$. Note that S_0, S_1, S_2, and S_3 represent the intensity of light, two linearly polarized components, and the circularly polarized light component, respectively. In the design of our nanoantennas, we can adjust the structural dimension L to alter the ratio of linearly polarized (S_1 and S_2) and circularly polarized (S_3) components, as illustrated in Fig. 2c. Specifically, we can measure all polarization states of light by adjusting the dimensions of the device, as shown in Supplementary Figs. 12–14 of Supplementary Note 3.

In actual testing, we chose to systematically explore the device which is sensitive only to the circular polarization component (S_3), as indicated by the dashed box in Fig. 2c. The collected photovoltage patterns that are highly consistent with the simulation, as shown in Supplementary Fig. 8. of Supplementary Note 2. Figure 2d shows the experimentally measured QWP angle-dependent photovoltages at

https://doi.org/10.1038/s41467-024-52632-8

wavelengths of 1.55 μm and 4 μm. Through fitting, it can be observed that the photocurrent varies with the QWP angle following a standard sine function relationship. This indicates that it effectively mitigates the impact of linear polarization components to a large extent, demonstrating excellent circular polarization sensitivity for detection. Furthermore, the functions for the two wavelengths exhibit opposite phases, enabling effective detection and discrimination from both the wavelength and circular polarization state perspectives. To gain a clearer understanding of the mechanisms and patterns of photocurrent generation, we conducted a 1.55 μm photocurrent mapping test on the device, as demonstrated in Supplementary Figs. 15–17 of Supplementary Note 4[39–41].

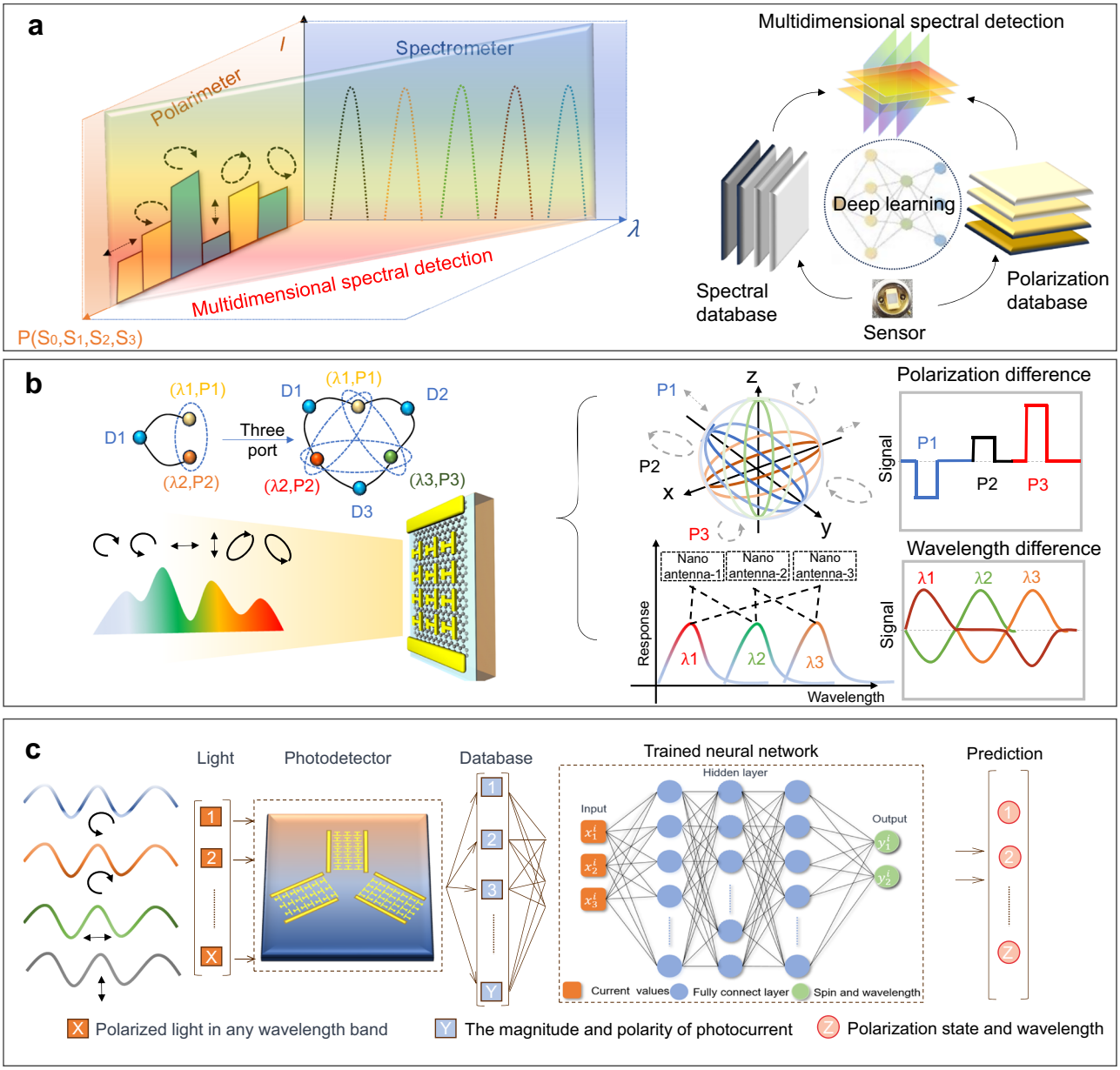

Fig. 1 | Overall approach of intelligent high-dimensional spectral detection. **a** The current photodetection methods can, at most, capture two-dimensional optical information within a three-dimensional parameter space encompassing intensity, polarization (stokes parameters $S_{0,1,2,3}$), and wavelength. Specifically, they are capable of measuring either the intensity and polarization at a fixed wavelength (polarimeter, depicted as a light yellow plane), or the intensity and wavelength at a fixed polarization state (spectrometer, illustrated as a light blue plane). Simultaneously detecting all three dimensions of parameters poses a significant challenge (spatially colorful slices). In our design proposal, the implementation of multidimensional spectral detection requires the integration of deep learning techniques with sensors capable of simultaneously detecting and distinguishing polarization and wavelength information. **b** A schematic diagram demonstrating a method for simultaneously sensing and processing both polarization and wavelength information of light. Graphene devices modified with nanoantennas exhibit varying photocurrent responses to light of two different wavelengths and polarizations, manifesting distinct amplitudes and polarities. This capability enables the differentiation of multidimensional information combinations. The three devices exhibiting responses to different wavelengths can be integrated into a three-port device. Through pairwise information mapping, this device can identify more combinations of wavelengths and polarizations. Polarization information ($P_{1,2,3}$) is deciphered from the measured ellipticity, while wavelength information ($\lambda_{1,2,3}$) is determined by the varying sizes of the nanoantennas. **c** Conceptual diagram of machine learning for the acquisition and identification of optical wavelength and polarization information using a three-port system. By training on the trends of photocurrents and utilizing neural networks, the recognition of polarization information for any wavelength of light can be achieved.

https://doi.org/10.1038/s41467-024-52632-8

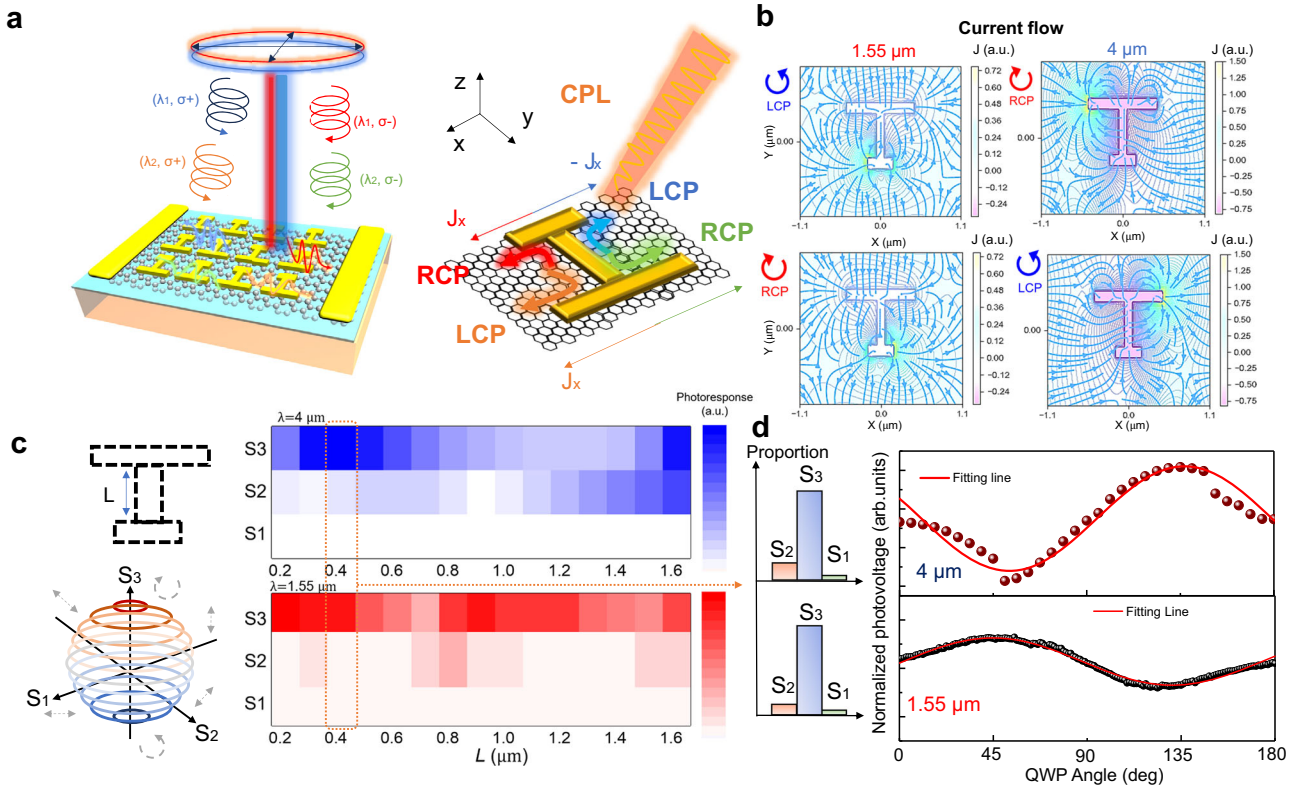

Fig. 2 | Sensor design with high-dimensional detection capability. a The dual-arm metasurface structure on graphene can localize light of different wavelengths and handedness on either side of the dual arms, generating vectorial photocurrents with varying magnitudes and directions. CPL, LCP, and RCP respectively represent circularly polarized light, left-handed circularly polarized light, and right-handed circularly polarized light. **b** Simulated near-field distribution and predicted vectorial photocurrent in a unit cell at different wavelengths and circular polarization states of incident light. J represents the current density formed by the near-field distribution. **c** The double-arm structure enables stokes parameters (S0,1,2,3) detection, where changing the arm length *L* allows realize the adjustment of the proportion of circularly polarized light components and linearly polarized light components. The orange dashed box represents the size most sensitive to the circular offset component (S3). **d** Experimentally measured QWP (quarter-wave plate) angle-dependent photovoltages under normally incident illumination at 1.55 μm and 4 μm wavelengths. The left subplot shows the proportion of S-parameters for the test device.

Based on the measured photoelectric signal, it is evident that the device exhibits photocurrent signals with different amplitudes and polarities for two different wavelengths (1.55 μm and 4 μm) and circular polarization states (LCP and RCP). In addition to demonstrating excellent detection capabilities for dual-wavelength circularly polarized light, this also a potential platform for applications in the fields of high-capacity photonics that can carry diverse information[42–47]. Here, optical information can offer multiple degrees of freedom by combining wavelength and chirality dimensions, and it can be encoded using easily distinguishable photocurrent amplitudes and polarities for the purpose of transcribing and decoding in optical communication. Figure 3a shows a schematic diagram of the photovoltage signal collection. Photovoltages were measured by a lock-in amplifier under illumination with LCP and RCP light, which was modulated by an optical chopper at 500 Hz.

Under the single-light incident mode, which means that only a beam carrying specific wavelength and polarization information is incident on the device, the corresponding photocurrent signal is obtained. When we encode it as “0”, “−1”, “1”, “−2”, or “2” according to the amplitude and polarity of the photovoltages, the wavelength and polarization information of the input light can be easily identified through the obtained output signals, as shown in Fig. 3b. The experimentally measured photovoltage signals corresponding to different encodings are shown in Fig. 3c. Different wavelengths and circular polarization information correspond to photovoltages with distinct amplitudes and polarities. Notably, the photovoltage amplitude at the 4 μm wavelength is approximately twice that at the 1.55 μm wavelength. Therefore, the photovoltage signals corresponding to the four different encodings are easily recognizable and distinguishable.

In addition to the single-light incident mode, this device can also be used for encoding and distinguishing in dual-light incident mode, where any two beams carrying wavelength and polarization information can be incident on the device. Encoding the interweaving of two different multidimensional information types by photovoltages is not overly complex. When the wavelength information is different but the circular polarization information is consistent, the photovoltage polarities are opposite, leading to subtraction of the photocurrent in dual-light coupling, resulting in a weaker signal, which can be encoded as “−1” and “1”. When both the wavelength and circular polarization information are different, the photovoltage polarities are the same, causing an accumulation of photocurrent in dual-light coupling, resulting in a larger photocurrent signal, which can be encoded as “−2” and “2”. When different circular polarization states of the same wavelength are coupled, the photovoltages cancel out, yielding a value of “0”, as displayed in Fig. 3d. The experimentally measured photovoltage corresponding to the encoding in dual-light incident mode is depicted in Fig. 3e, demonstrating stable optical computing capabilities.

Design of the three-port device

The successful detection of dual-wavelength circularly polarized light by the double-armed structure indicates that by adjusting the sizes of the double arms, it is possible to achieve circular polarization

https://doi.org/10.1038/s41467-024-52632-8

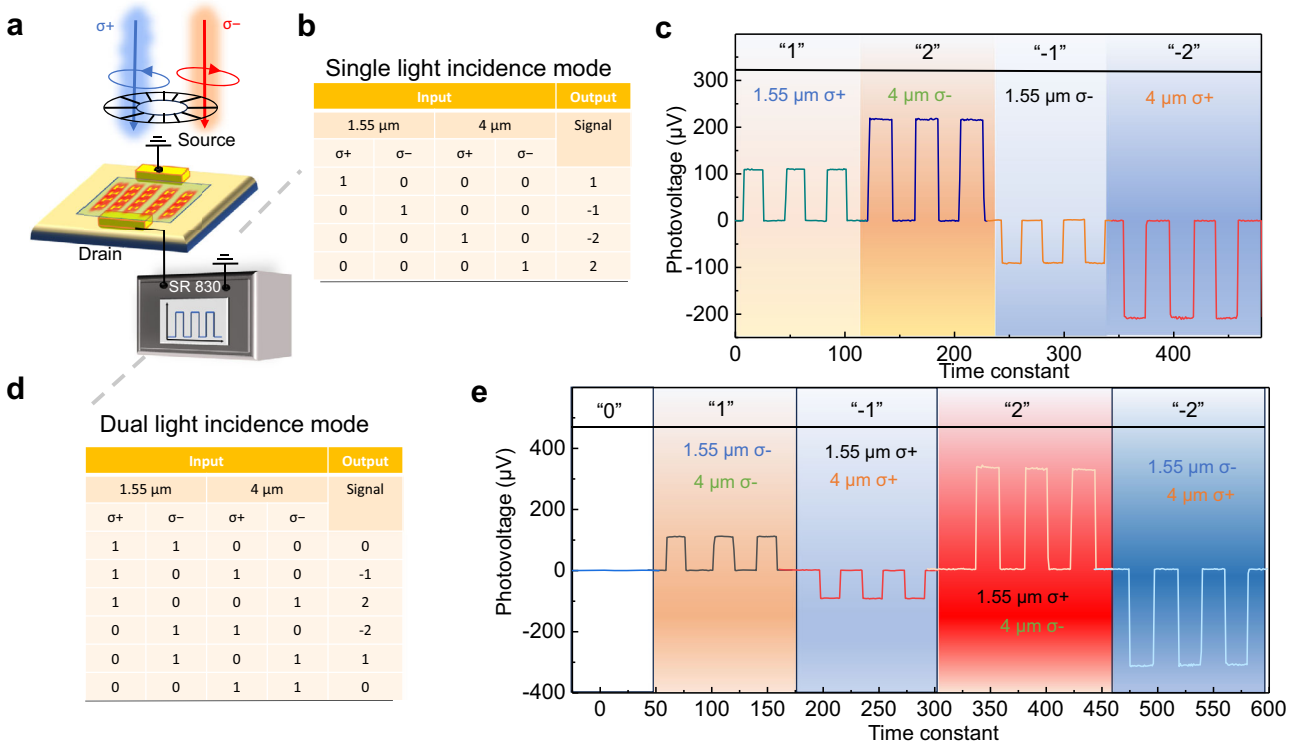

Input				Output
1.55 μm		4 μm		Signal
σ+	σ−	σ+	σ−	
1	0	0	0	1
0	1	0	0	-1
0	0	1	0	-2
0	0	0	1	2

Input				Output
1.55 μm		4 μm		Signal
σ+	σ−	σ+	σ−	
1	1	0	0	0
1	0	1	0	-1
1	0	0	1	2
0	1	1	0	-2
0	1	0	1	1
0	0	1	1	0

Fig. 3 | Optical encoding for high-dimensional information identification. **a** Schematic diagram of the optical information encoding device. Under uniform illumination at 1.55 μm and 4 μm wavelengths with LCP and RCP, photovoltages are measured at zero external bias (Vd = Vg = 0 V). **b** Optical information encoding in single light incidence mode. The input signals, which can be either 1.55 μm LCP, 1.55 μm RCP, 4 μm LCP, or 4 μm RCP, are converted into output photovoltage signals. These output signals are encoded as "1" for positive polarity and amplitude, "−1" for negative polarity and amplitude, "2" for positive polarity and higher amplitude, and "−2" for negative polarity and higher amplitude. **c** Corresponding encoded photovoltage output signal in single light incidence mode. Different colored backgrounds represent the photoelectric switch signals corresponding to different output signals. **d** Optical information encoding in dual light incidence mode. The input signals consist of any two beams of light, each carrying circular polarization and wavelength information. Based on the polarity and amplitude of their output photovoltage, these signals can be encoded as "0", "−1", "1", "−2" and "2". **e** Corresponding encoded photovoltage output signal in dual light incidence mode.

detection for any two wavelengths. Furthermore, dual-wavelength circular polarization detection offers four information channels for optical communication, considering the two dimensions of wavelength and polarization states (2 wavelengths × 2 polarization states = 4 optical channels). These four types of information can be precisely distinguished based on the two-dimensional photocurrent mapping composed of the magnitude and polarity of the photocurrent collected by a single device, as illustrated in the left subplot of Fig. 4a. If we boldly expand the device ports of nanoantennas with different sizes as the third dimension of the two-dimensional photocurrent mapping, we can obtain a spatial photocurrent mapping model as depicted in the right subplot of Fig. 4a. This allows us to precisely distinguish more wavelengths and their polarization information.

Therefore, by adjusting the structural parameters, we designed a three-port device, as shown in Fig. 4b, for the purpose of three-wavelength circular polarization detection. Such a three-port layout is also beneficial for ensuring that the circular light spot can cover all the devices, making full use of the available space. Among them, we used plasmonic nanostructure arrays for circular polarization detection at 1.55 μm and 4 μm, 1.55 μm and 7 μm, and 4 μm and 7 μm as three different ports, named "1.55-4," "1.55-7," and "4-7", respectively. By individually applying circularly polarized light of the corresponding wavelengths to each of the three ports, we measured the relationship between the photocurrent and the QWP angle, as shown in Fig. 4c. The photovoltages obtained at each port exhibit a perfect sinusoidal relationship with the QWP angle, demonstrating excellent dual-wavelength circular polarization detection capabilities for each port.

Importantly, each port is sensitive only to the two specific wavelength bands designed for it and does not respond to the third wavelength band. Consequently, there is no interference between the ports. This can be verified by conducting 1.55 μm photocurrent scanning mapping on a three-port device, as shown in Fig. 4d. It can be observed from the photocurrent scanning maps for the 1.55-4 and 1.55-7 ports that LCP and RCP light induce photocurrent distributions with completely opposite polarities. However, for ports 4-7, there is no difference in the photocurrent distribution between LCP and RCP illumination, and the net photocurrent within the channel is close to zero. The stable switch photovoltage signals of the corresponding ports under LCP and RCP light at 1.55 μm, 4 μm, and 7 μm are shown in Supplementary Fig. 10 of Supplementary Note 2. Each device can ensure long-term operational stability while achieving low noise and fast response speed to ensure signal stability (see Supplementary Figs. 18–21, and Supplementary Tables 1 and 2 in Supplementary Note 5). Even though the responsivity of device does not show significant advantages compared to typical and commercial zero-bias infrared detectors (see Supplementary Table 3), we can attempt to apply gate voltage and modify the device layout to further enhance its responsivity (see Supplementary Figs. 22 and 23 of Supplementary Note 5). Three-port devices will have more encoding modes and data capacity. When a beam of light carrying both wavelength and spin information is incident on the device, the incident light spot will cover the entire region of the three-port device. Three sets of photoelectric voltage signals from a three-port device are collected by three testing channels. These signals are encoded as "0," "±1," and "±2" based on their polarity and amplitude. Therefore, the combination of output

https://doi.org/10.1038/s41467-024-52632-8

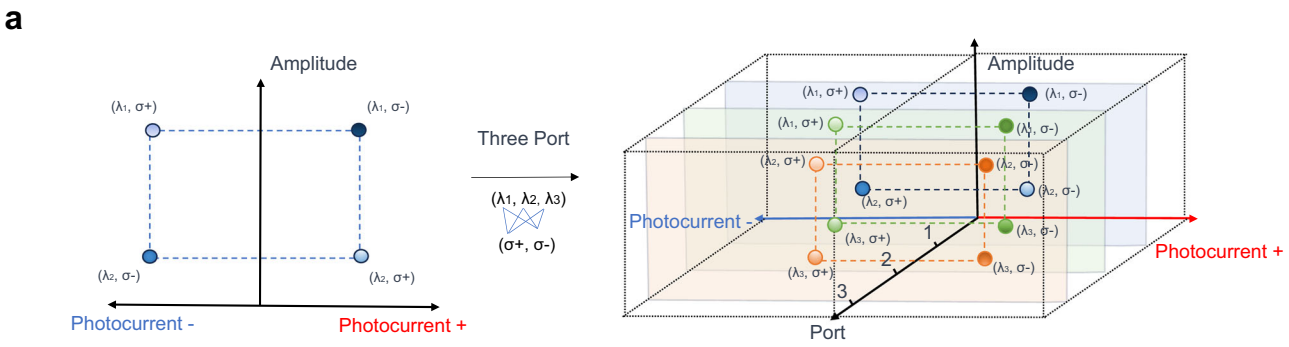

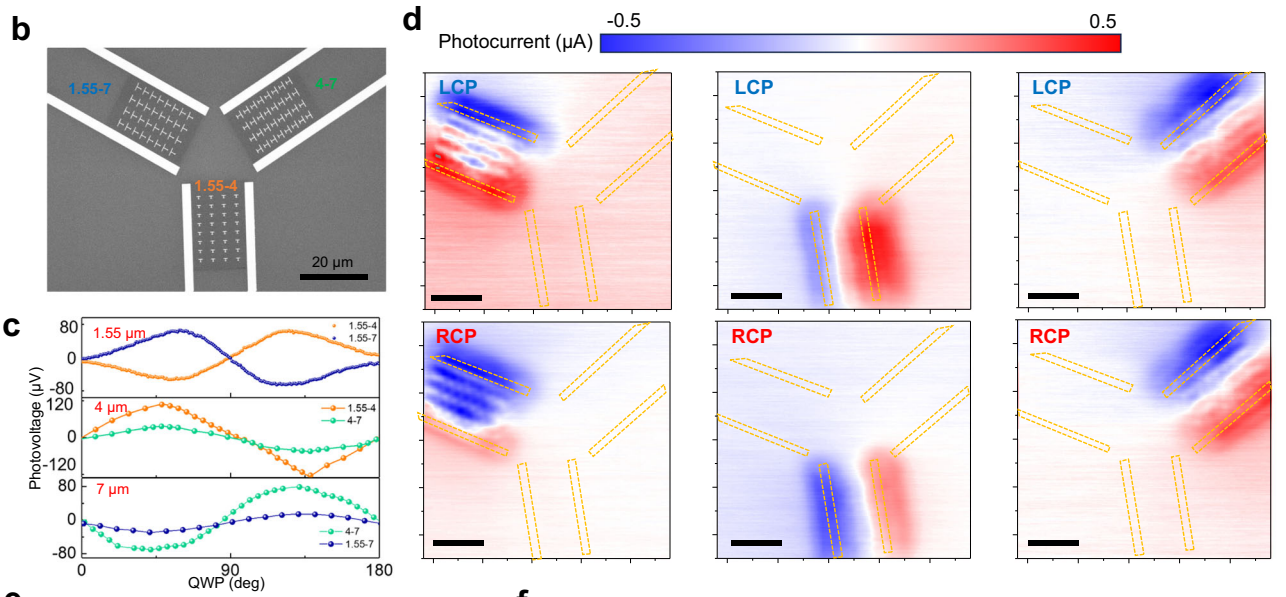

e

Input						Output		
1.55 μm		4 μm		7 μm		Signal		
σ+	σ−	σ+	σ−	σ+	σ−	D1	D2	D3
1	0	0	0	0	0	-1	0	2
0	1	0	0	0	0	1	0	-2
0	0	1	0	0	0	-2	1	0
0	0	0	1	0	0	2	-1	0
0	0	0	0	1	0	0	-2	1
0	0	0	0	0	1	0	2	-1

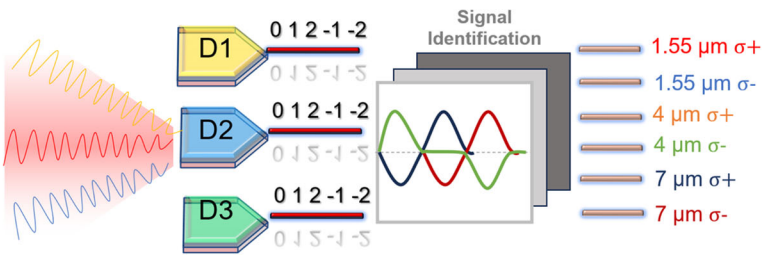

Fig. 4 | Three-port design for three-band circular polarization detection. **a** Construction of the spatial model of the photocurrent. For a single-port device, it's possible to determine both the wavelength and spin information of light within a two-dimensional plane formed by the magnitude and amplitude of the photocurrent. Through the cooperative action of multiple devices, it is possible to establish a spatial photocurrent model with wavelength and spin resolution capabilities. **b** Scanning electron microscope image of a three-port graphene device. Based on its resonant dual-band characteristics, it can be divided into 1.55-4 port, 1.55-7 port, and 4-7 port configurations. **c** Experimentally measured QWP angle-dependent photovoltages of three ports under incident illumination at 1.55 μm, 4 μm and 7 μm wavelengths. **d** Photocurrent scanning mapping for three ports under illumination of 1.55 μm in LCP and RCP light. The photocurrent scanning maps at ports 1.55-4 and 1.55-7 exhibit opposite current distributions for 1.55 μm LCP and RCP, whereas there is no distinction at ports 4-7. The black scale bar represents 20 μm. The orange dashed box represents the shape of the electrode. **e** Photovoltage encoding generated by the incidence of circularly polarized light with three different wavelengths. The combination of output signals from each channel allows for the identification of the wavelength and polarization information of the incident light. **f** Schematic representation of the extraction of three-wavelength circularly polarized signals. In the case of mixed light incidence, the processing of photovoltage signal encoding allows for the extraction of the wavelength and circular polarization information of the incident light.

signals from the three optical channels allows for the unique determination of the wavelength and spin information of the incident light, as displayed in Fig. 4e. Similarly, in multilight incidence mode, the wavelength and polarization information of light can be determined by encoding and distinguishing the amplitude and polarity of the collected photovoltage signals (Fig. 4f). Additionally, each port device can operate in multiple light incidence modes, leading to signal superposition and cancellation, which provides the potential for implementing optoelectronic logic gates (Supplementary Fig. 24 of Supplementary Note 5).

Machine learning mechanisms for three-port devices

Applying machine learning to the processing of three-port information can help us establish intelligent high-dimensional detectors with

https://doi.org/10.1038/s41467-024-52632-8

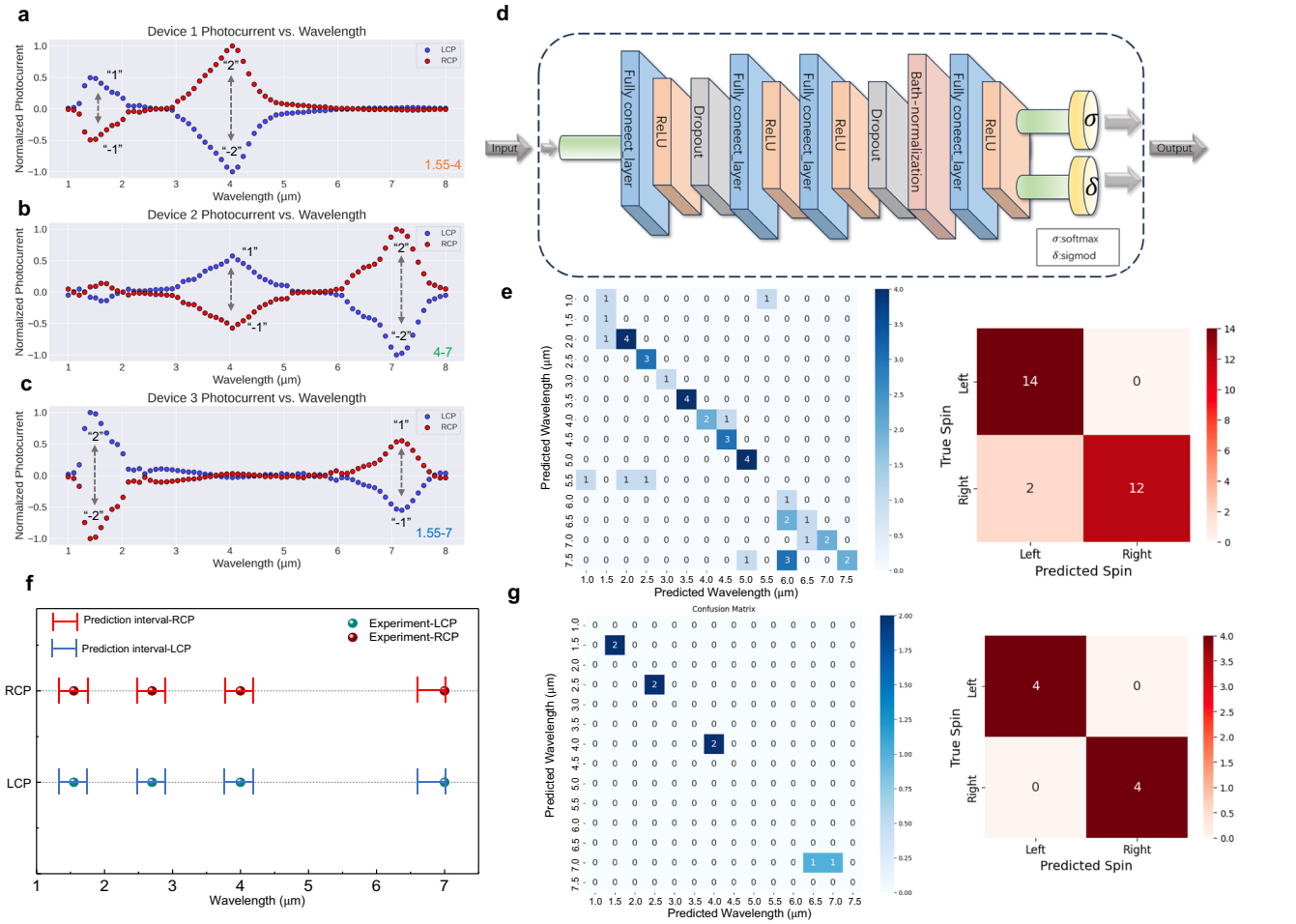

Fig. 5 | Implementation of intelligent spin spectrum detectors based on machine learning mechanisms for three-port devices. a–c Predicted photocurrent of a three-port device under different wavelengths for LCP and RCP incident light based on a simulation model that closely fits the experimental data. **d** A potential neural network structure diagram for training, testing, and predicting spin information and wavelength. The multilayer perceptron neural network model typically consists of an input layer, an output layer, and several hidden layers. Each hidden layer includes a fully connected layer and some layers designed to optimize the model, such as dropout layers and batch-normalization layers. In real model training and prediction, we use the ReLU activation function in the hidden layers. For the output layer, we have adopted the Sigmoid and Softmax functions as appropriate activation functions to better adapt to the network's training and prediction purposes. **e** A confusion matrix generated based on the neural network model's predictions of wavelength (left subplot) and spin (right subplot) information on the test set, which comes from the simulation dataset. The numbers on the diagonal represent the count of accurately identified samples, while the numbers off the diagonal indicate the count of incorrectly predicted samples. **f** The prediction results of a set of real laboratory data on our constructed neural network model. The solid spheres represent experimental data, and the line segment intervals represent the prediction intervals of the model. **g** The confusion matrix drawn based on the prediction results of this set of real laboratory data. For the eight collected samples, our neural network model can accurately predict wavelength (left subplot) and spin information (right subplot).

discernment and predictive capabilities[48–50]. With an exceptionally high level of conformity between experimental testing and simulated trends, we endeavor to use simulated data as an example to predict the photoelectric current trends of a three-port device under ultrabroadband (1–8 μm) circularly polarized light through machine learning. This endeavor aims to achieve the extraction of spin information from arbitrary spectral bands under ultrabroadband conditions. Figure 5a–c shows the simulated photocurrent trends of the "1.55-4," "1.55-7," and "4-7" three-port devices, respectively, in response to circularly polarized light with wavelengths ranging from 1 to 8 μm.

We applied multilayer perceptron (MLP) to predict the wavelength and polarization state of the corresponding photocurrent here. We employ supervised learning techniques to train an MLP neural network consisting of fully connected neurons with a nonlinear kind of activation function organized in multiple layers to distinguish data that are obviously not linearly separable in our dataset. The architecture of the neural network is formalized as follows[51]:

$$\mathbb{N}:\left\{(I_1,I_2,I_3)_i,(S,\lambda)_i\right\}\overset{yields}{\rightarrow}\left\{\left(\hat{S},\hat{\lambda}\right)_i\right\} \tag{1}$$

Here, I_i represents the photocurrent values detected from the three-port device under ultrabroadband, where $(I_1,I_2,I_3)_i$ denotes the i^{th} group of photocurrent values in our dataset. The term S is the spin label associated with the photocurrent, which provides information about the left circular polarization (LCP) or right circular polarization (RCP) of the device. λ pertains to the wavelength associated with the photocurrent, $(S,\lambda)_i$ is the label for the i^{th} photocurrent, and $\left(\hat{S},\hat{\lambda}\right)_i$ is the prediction outcome of the network.

The neural network designed for the prediction of spin information and wavelength is a multi-input multi-output (MIMO) model with multiple layers of neurons (Fig. 5d), where neurons in the L^{th} layer only accept the output from the $(L-1)^{th}$ layer and only project to the

$(L+1)^{th}$ layer.

$$\begin{aligned} r^1 &= I,\ I \in R^{n\times d} \\ r^L &= f\left(W^L r^{L-1} + b^L\right), 1 < L < N \\ y_i &= g_i(W^N r^{N-1} + b^N) \end{aligned} \tag{2}$$

Here, I is the input stored in the shape of an $R^{n\times d}$ matrix from a specific dataset collected by a photodetector, r^L denotes the neural activity in the L^{th} layer, and W^L is the connection matrix from $(L-1)^{th}$ to the L^{th} layer. $f(\cdot),g(\cdot)$ are (usually nonlinear) activation functions of the model. The output of the network is read through connections W^N. Parameters b^L and b^N are the biases for the hidden layers and output units, respectively. We utilize the Sigmoid function as an activation function to classify the polarization information of the input photocurrent values while using SoftMax as the activation function for wavelength prediction.

In our study, we methodologically reformulated wavelength prediction as a category task, which permits our model to estimate the corresponding wavelength for any given input with an error margin that is maintained below the 0.5 μm threshold (Supplementary Figs. 25 and 26 of Supplementary Note 6). We elaborately design a combination cost function for multiple output tasks as follows:

$$Cost = \alpha_1 \parallel S - \hat{S}\parallel^2 + \alpha_2 \parallel \lambda - \hat{\lambda}\parallel^2 + \beta\|W\|_2^2 \tag{3}$$

where α_1,α_2 are weighting factors that balance the contribution of each loss component to the total cost, $\beta\|W\|_2^2$ is the L2 regularization equation and β is the regularization factor. To enhance network optimization, several traditional optimization algorithms, such as the Adam optimization algorithm, which is celebrated for its adaptive learning rate features, were chosen to improve the model's performance. Upon completion of the training phase, a neural network model is acquired that is capable of predicting the polarization state and wavelength for a set of valid photocurrent values[52]. As shown in Supplementary Table 4 of Supplementary Note 6, our machine learning model achieved satisfactory results for the prediction of spin and wavelength based on the simulated database. The prediction of the wavelength for the input photocurrent set is shown in Fig. 5e, and the diagonal entries of the confusion matrix represent the number of accurate predictions. The detailed information of the model workflow is shown as Supplementary Fig. 27 of Supplementary Note 6.

Ideally, when we test our device with circularly polarized light of arbitrary wavelengths (1.55 μm, 2.7 μm, 4 μm and 7 μm), the predicted results from the model closely match the actual values, as shown in Fig. 5f, g. This validates the feasibility of our approach.

Discussion

We have demonstrated a high-dimensional spin spectrometer capable of deciphering complex spectral information of arbitrary spin light across an ultra-wide band. While the demonstration was conducted under circular polarization, the geometric design of the metasurface has been proven to simultaneously detect linearly and circularly polarized light. Essentially, we can detect information from any polarization state. It is worth noting that our approach offers advantages compared to natural materials. With the assistance of machine learning, utilizing the dispersion and anisotropy of natural materials enable the generation of necessary training data points for light under various incident conditions during the training process. However, the distinguishability of natural materials has boundaries, leading to certain functional limitations. Here, our metasurface design can overcome this inherent issue in natural materials, possessing adjustable and sufficiently significant discriminative capability. Additionally, our device fabrication process is simple and well-established, offering better controllability and reproducibility compared to heterojunction and twist systems. Therefore, applying machine learning to our metasurface design scheme exhibits robust learning and precise discrimination capabilities, enabling us to achieve high-dimensional spectral detection using conventional methods without the need for complex material systems or cumbersome processing techniques. A detailed comparison with existing work can be found in Supplementary Table 5.

Based on the exploration presented in this work, there are still some problems that need further investigation to resolve. For example, regarding responsivity, performance can be further enhanced by applying gate voltage, improving material quality, and optimizing device layout. Additionally, to further enhance integration, single-unit devices can be expanded into array pixel devices, enabling multi-channel signal output and further reducing time resolution.

Methods

Device fabrication

The graphene sample preparation involved mechanically exfoliating graphene onto a silicon substrate with a 285 nm thick layer of silicon dioxide (heavily p-doped silicon wafer). Suitable graphene flakes were then selected under an optical microscope, and their coordinates were recorded. The graphene flakes are marked using electron beam lithography (EBL) to create corresponding markers on the silicon substrate. (EBL, JBX-6300FS, Jeol; PMMA, A5; spin-coating speed of 4000 rpm; development with MIBK: IPA = 1:3 for 30 s, followed by IPA rinsing for 30 s.) The markers are metalized using AJA Ebeam Evaporator deposition of 5 nm Ti and 50 nm Au, followed by a lift-off process with acetone at 65 °C for 2 h and an IPA rinse for 10 min. Graphene patterning is achieved by spin-coating the sample with PMMA following the parameters from step one, using EBL to define the areas for graphene etching, developing the pattern, plasma etching the exposed graphene (O_2 gas 20 sccm, power 20 W, duration 30 s), removing the PMMA with acetone, and then rinsing the acetone with IPA. Nanostructures and electrodes are fabricated using EBL to define the patterns, followed by thermal deposition of 5 nm Pd and 60 nm Au and a lift-off process.

Characterization methods

We utilized quantum cascade lasers with wavelengths of 4 μm and 6–8 μm as excitation sources and directed the light onto the device base using a mirror and an off-axis parabolic mirror, which then transmitted the light onto the device. We used quarter-wave plates with wavelengths of 4 μm and 7 μm to modulate circularly polarized light. The device's source and drain contacts were connected to a lock-in amplifier, which was also connected to a chopper placed at the laser output to ensure the output of the light signal, and the lock-in amplifier signal output was controlled using a program written in Labview.

For the 1550 nm photocurrent scanning mapping setup, the 1550 nm laser is directed by a single-mode fiber to the homemade setup. The light passes through a lens, a polarizer, and a quarter-wave plate. The laser beam is focused by an objective into a submicrometer diameter on the sample surface. For the electrical measurement setup, the longitudinal voltage and gate voltage are applied using a Keithley 2604B source meter. An FS Pro Integrated Semiconductor Parameter Testing System (Noise Analyzer) is used to measure the photocurrent, noise, and resistance of devices.

Simulation

The optical responses of dual-arm plasma nanostructures on graphene were simulated with a single unit and applying periodic boundary conditions using the finite-difference time-domain method (FDTD Solutions package, Lumerical). The light source was a plane wave with normal incidence from the air. The boundaries above and below the array of the diamond flower structure were perfectly matched layers. The mesh spacings were less than 10 nm in all dimensions. From

bottom to top, the simulated structure consists of a silicon substrate, SiO_2 (300 nm thickness), a gold metasurface (20 nm thickness) and air. The photocurrent is calculated based on the hydrodynamic photocurrent model in Matlab using the near-field distribution extracted by FDTD.

Data availability

All the technical details for producing the figures are provided in the supplementary information. The data are available from the corresponding authors C.-W.Q. or W.B.G. upon request.

Code availability

All the technical details for implementing the simulation are provided in the Supplementary Information. The code for this study is available in GitHub (https://doi.org/10.5281/zenodo.13762816).

References

1. Yi, L., Hou, B., Zhao, H. & Liu, X. X-ray-to-visible light-field detection through pixelated colour conversion. *Nature* **618**, 281–286 (2023).
2. Yang, Z. et al. Single-nanowire spectrometers. *Science* **365**, 1017–1020 (2019).
3. Akinwande, D. et al. Graphene and two-dimensional materials for silicon technology. *Nature* **573**, 507–518 (2019).
4. Chen, Z. & Segev, M. Highlighting photonics: looking into the next decade. *eLight* **1**, 2 (2021).
5. Liu, C. et al. Two-dimensional materials for next-generation computing technologies. *Nat. Nanotechnol.* **15**, 545–557 (2020).
6. Gansel, J. K. et al. Gold helix photonic metamaterial as broadband circular polarizer. *Science* **325**, 1513–1515 (2009).
7. Zhao, Y., Belkin, M. A. & Alù, A. Twisted optical metamaterials for planarized ultrathin broadband circular polarizers. *Nat. Commun.* **3**, 870 (2012).
8. Bao, Y., Wen, L., Chen, Q., Qiu, C.-W. & Li, B. Toward the capacity limit of 2D planar Jones matrix with a single-layer metasurface. *Sci. Adv.* **7**, 1–7 (2021).
9. Koepfli, S. M. et al. Metamaterial graphene photodetector with bandwidth exceeding 500 gigahertz. *Science* **380**, 1169–1174 (2023).
10. Wei, J. X., Xu, C., Dong, B. W., Qiu, C. W. & Lee, C. K. Mid-infrared semimetal polarization detectors with configurable polarity transition. *Nat. Photonics* **15**, 614 (2021).
11. Wei, J. X. et al. Zero-bias mid-infrared graphene photodetectors with bulk photoresponse and calibration-free polarization detection. *Nat. Commun.* **11**, 6404 (2020).
12. Jiang, H. et al. Ultrahigh Photogain Short-Wave Infrared Detectors Enabled by Integrating Graphene and Hyperdoped Silicon. *ACS nano* **16**, 12777–12785 (2022).
13. Jiang, H. et al. Synergistic-potential engineering enables high-efficiency graphene photodetectors for near- to mid-infrared light. *Nat. Commun.* **15**, 1225 (2024).
14. Jiang, H. et al. Ultrasensitive and fast photoresponse in graphene/silicon-on-insulator hybrid structure by manipulating the photogating effect. *Nanophotonics* **9**, 3663–3672 (2020).
15. Jiang, H. et al. Enhanced Photogating Effect in Graphene Photodetectors via Potential Fluctuation Engineering. *ACS Nano* **16**, 4458–4466 (2022).
16. Liu, W. et al. Graphene charge-injection photodetectors. *Nat. Electron.* **5**, 281–288 (2022).
17. Grotevent, M. J. et al. Integrated photodetectors for compact Fourier-transform waveguide spectrometers. *Nat. Photonics* **17**, 59–64 (2023).
18. Feng, Z. et al. Dual-band polarized upconversion photoluminescence enhanced by resonant dielectric metasurfaces. *eLight* **3**, 21 (2023).
19. Tang, X., Ackerman, M. M., Chen, M. & Guyot-Sionnest, P. Dual-band infrared imaging using stacked colloidal quantum dot photodiodes. *Nat. Photonics* **13**, 277–282 (2019).
20. Jiang, H. et al. Gate modulation enhanced position-sensitive detectors using graphene/silicon-on-insulator structure. *Carbon* **184**, 445–451 (2021).
21. Yuan, S., Naveh, D., Watanabe, K., Taniguchi, T. & Xia, F. A wavelength-scale black phosphorus spectrometer. *Nat. Photonics* **15**, 601–607 (2021).
22. Yoon, H. H. et al. Miniaturized spectrometers with a tunable van der Waals junction. *Science* **378**, 296–299 (2022).
23. Deng, W. et al. Electrically tunable two-dimensional heterojunctions for miniaturized near-infrared spectrometers. *Nat. Commun.* **13**, 4627 (2022).
24. Yang, Z., Albrow-Owen, T., Cai, W. & Hasan, T. Miniaturization of optical spectrometers. *Science* **371**, eabe0722 (2021).
25. Xiong, Y. et al. Twisted black phosphorus–based van der Waals stacks for fiber-integrated polarimeters. *Sci. Adv.* **8**, eabo0375 (2022).
26. Rubin, N. A. et al. Matrix Fourier optics enables a compact full-Stokes polarization camera. *Science* **365**, eaax1839 (2019).
27. Ma, C. et al. Intelligent infrared sensing enabled by tunable moiré quantum geometry. *Nature* **604**, 266–272 (2022).
28. Fan, Y. et al. Dispersion-assisted high-dimensional photodetector. *Nature* **630**, 77–83 (2024).
29. Yuan, S. et al. Geometric deep optical sensing. *Science* **379**, eade1220 (2023).
30. Hentschel, M., Schäferling, M., Duan, X., Giessen, H. & Liu, N. *Chiral Plasmon. Sci. Adv.* **3**, 1–13 (2017).
31. Chen, Y. et al. Multidimensional nanoscopic chiroptics. *Nat. Rev. Phys.* **4**, 113–124 (2021).
32. Long, G. et al. Chiral-perovskite optoelectronics. *Nat. Rev. Mater.* **5**, 423–439 (2020).
33. Wei, J. et al. Geometric filterless photodetectors for mid-infrared spin light. *Nat. Photonics* **17**, 171–178 (2023).
34. Gabor, N. M. et al. Hot carrier-assisted intrinsic photoresponse in graphene. *Science* **334**, 648–652 (2011).
35. Sun, D. et al. Ultrafast hot-carrier-dominated photocurrent in graphene. *Nat. Nanotechnol.* **7**, 114–118 (2012).
36. Woessner, A. et al. Near-field photocurrent nanoscopy on bare and encapsulated graphene. *Nat. Commun.* **7**, 10783 (2016).
37. Zuev, Y. M., Chang, W. & Kim, P. Thermoelectric and magnetothermoelectric transport measurements of graphene. *Phys. Rev. Lett.* **102**, 096807 (2009).
38. Pettine, J. et al. Light-driven nanoscale vectorial currents. *Nature* **626**, 984–989 (2024).
39. Park, J., Ahn, Y. H. & Ruiz-Vargas, C. Imaging of photocurrent generation and collection in single-layer graphene. *Nano Lett.* **9**, 1742–1746 (2009).
40. Chen, S. et al. Electron optics with p-n junctions in ballistic graphene. *Science* **353**, 1522–1525 (2016).
41. Song, J. C. W. & Levitov, L. S. Shockley-Ramo theorem and long-range photocurrent response in gapless materials. *Phys. Rev. B* **90**, 075415 (2014).
42. Zhang, Y. et al. Chirality logic gates. *Sci. Adv.* **8**, eabq8246 (2022).
43. Kim, W. et al. Perovskite multifunctional logic gates via bipolar photoresponse of single photodetector. *Nat. Commun.* **13**, 720 (2022).
44. Liu, S. et al. Bi2O3 Layer-Integrated, Double-Sided Responsive, Waveband-Discriminated Perovskite Photodetector for Encrypted Optical Communication. *Adv. Optical Mater.* **11**, 2300831 (2023).
45. Wang, D. et al. Observation of polarity-switchable photoconductivity in III-nitride/MoSx core-shell nanowires. *Light Sci. Appl.* **11**, 227 (2022).

46. Wu, P. et al. Two-dimensional transistors with reconfigurable polarities for secure circuits. *Nat. Electron.* **4**, 45–53 (2021).
47. Kwak, D., Polyushkin, D. K. & Mueller, T. In-sensor computing using a MoS2 photodetector with programmable spectral responsivity. *Nat. Commun.* **14**, 4264 (2023).
48. Li, T. et al. Reconfigurable, non-volatile neuromorphic photovoltaics. *Nat. Nanotechnol.* **18**, 1303–1310 (2023).
49. Mennel, L. et al. Ultrafast machine vision with 2D material neural network image sensors. *Nature* **579**, 62–66 (2020).
50. Lee, S., Peng, R., Wu, C. & Li, M. Programmable black phosphorus image sensor for broadband optoelectronic edge computing. *Nat. Commun.* **13**, 1485 (2022).
51. Rosenblatt, F. The perceptron: A probabilistic model for information storage and organization in the brain. *Psychological Rev.* **65**, 386–408 (1958).
52. Jiang, H. et al. Machine learning code of metasurface-enabled broadband multidimensional photodetectors. https://doi.org/10.5281/zenodo.13762816 (2024).

Acknowledgements

We acknowledge the Singapore National Research Foundation and ASTAR through the Competitive Research Program (CRP Award No. NRF-CRP22–2019-0004 and NRF-CRP30–2023-0003), QEP Grants (NRF2021-QEP2-01-P01, NRF2021-QEP2-01-P02, NRF2021-QEP2-03-P01, NRF2021-QEP2-03-P10, NRF2021-QEP2-03-P11, NRF2021-QEP2-03-P09), IRG (M21K2c0116, M22K2c0088), the National Key Research and Development Program of China (Grant No. 2023YFB3611400), and the National Natural Science Foundation of China (Grant Nos. 62174026, 62225404, 61927808, 12004072). C.-W.Q. is also supported by the Competitive Research Program Award (NRF-CRP22–2019-0006 & NRF-CRP26–2021-0004) from the NRF, Prime Minister's Office, Singapore.

Author contributions

H.J., W-b.G and C.-W.Q. conceived the project. H.J., Y.C., and Y.Z. performed the measurements. H.J. and Y.C. fabricated the devices. H.J. and W.G. analyzed the data. H.J. performed the theoretical analysis. H.J., C.-W.Q and W.-b.G. wrote the manuscript. C.-W.Q. and W-b.G. supervised the project. R.Z., M.G., F.Z., Z.N., J.L. contributed to the discussion of the results.

Competing interests

The authors declare no competing interests.

Additional information

Supplementary information The online version contains supplementary material available at https://doi.org/10.1038/s41467-024-52632-8.

Correspondence and requests for materials should be addressed to Junpeng Lu, Cheng-Wei Qiu or Weibo Gao.

Peer review information *Nature Communications* thanks Hoon Hahn Yoon and the other, anonymous, reviewers for their contribution to the peer review of this work. A peer review file is available.